# Ubiquity of the Micrometer-Thick Interface along a Quartz–Water Boundary

Armin Mozhdehei, Lionel Mercury, Aneta Slodczyk

LANGMUIR

pubs.acs.org/Langmuir Article

# Ubiquity of the Micrometer-Thick Interface along a Quartz−Water Boundary

Armin Mozhdehei,* Lionel Mercury, and Aneta Slodczyk

Cite This: https://doi.org/10.1021/acs.langmuir.4c00742 Read Online



**ABSTRACT:** Water−rock interactions determine how the geochemical cycles revolve from the Earth's surface to the deep interior (large $T-P$ intervals). The underlying mechanisms interweave the fluxes of matter, time, and reactivity between fluid phases and solids. The deformation processes of crustal rocks are also known to be significantly affected by the presence or absence of water, typically with the hydrolytic weakening of quartz, olivine, and other silicate minerals. In fact, fluid−rock interactions mechanistically unfold along their interfaces, developing over a certain thickness within the two phases. Diffraction-limited mid-infrared microspectroscopy was employed to monitor the thermodynamic characteristics of liquid water along a quartz boundary. The hyperspectral Fourier transform infrared data set displayed a very strong distance-dependent signature for water over a 1 ± 0.5 $\mu$m thickness, while quartz appears unmodified, which is consistent with recent studies. This unexpected thick interface is tested against the geometry of the inclusion, the chemistry of the occluded liquid (especially pH), and the thermal conditions ranging from room temperature to 155 °C. Throughout this range of physicochemical conditions, the micrometer-thick interface is characterized by a ubiquitous, significant shift in the Gibbs free energy of water inside the interfacial layer. This conclusion suggests that the interface-imprinting phenomenon driving this microthick layer has thermodynamic roots that give rise to specific properties along the quartz−water interface. This finding questions the systematic use of the bulk phase data sets to evaluate how water−rock interactions progress in porous media.

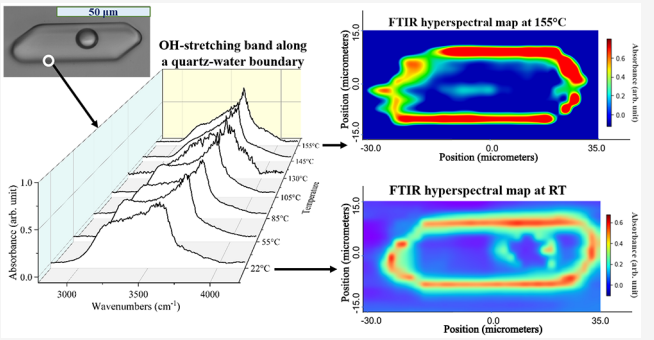




## 1. INTRODUCTION

The evolution of large hydrosystems through time and being subjected to climate change or anthropogenic activities is rooted in water−rock interactions at the pore scale. Apart from controlling the composition of the liquid phase, water−rock interactions are of utmost importance for driving the porosity accessible to flow. Mass balances from the global scale to the local scale, for understanding planetary geodynamics and optimizing geothermal doublets, require an understanding of how the driving force is controlled when both solid and dissolved phases come into contact. The standard approach to quantifying the driving forces uses the chemical potentials of the thermodynamically stable bulk phases. Measuring or even observing water−rock interactions at the pore scale in the field is of course impossible; consequently, many hypotheses are classically taken for granted to make calculations, typically with modeling intended for environmental diagnoses or predictivity.

The first parameter that has been under debate is the surface area of the liquid−solid contacts, triggered by many contradictory results between field-based and laboratory-based mineral solubilities.[1−4] Numerous explanations regarding the gap between these data sets are associated with the limited understanding of the relationship between the physical attributes and what is termed the "reactive" surface area of solids.[1−7] The second parameter that might be used to better quantify water−rock interactions is the pore size holding the reactions with counterintuitive observables or interpretations putting a size threshold from normal to pore size marked behavior around 1 $\mu$m.[8−12] This is surprising because the initial expectation focused on the nanometric pore size.[13] The third player in the water−mineral interactions is related to solid surface chemistry (i.e., hydrophilic vs hydrophobic properties). Zheng et al. showed that hydrophilic interfaces can create a solute-exclusion zone at their immediate periphery similar to liquid crystals.[14] The authors proposed that there is a long-range restriction of water molecules nucleating at the interface, leading to mobility-limited water.[14] Stack et al. focused on pore-scale reactivity, showing that carbonate precipitation occurs exclusively in macropores (>1 $\mu$m) within hydrophilic pores, while precipitation in both nanopores (<1 $\mu$m) and

Received: February 29, 2024
Revised: May 26, 2024
Accepted: June 5, 2024

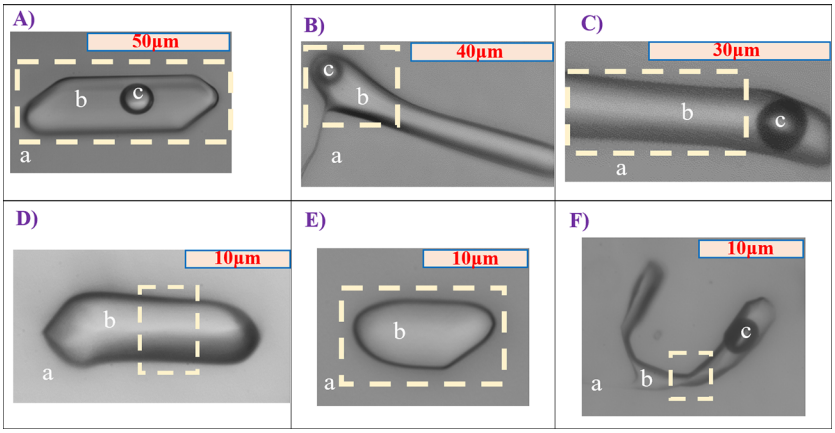


**Figure 1.** Micrographic images of SFIs located in the quartz fragment, including three distinct phases: (a) solid (quartz), (b) liquid (water or NaOH solution), and (c) gas (bubble of saturated water vapor). Among these, three SFIs labeled as (A) SFI-1, (B) SFI-2, and (C) SFI-3 contain water, while the remaining three SFIs trap an aqueous solution of NaOH at concentrations of (D) 0.5 M (SFI-4), (E) 1 M (SFI-5), and (F) 2 M (SFI-6). The rectangular dashed lines show the IR acquisition areas for each SFI.

macropores was observed in hydrophobic pores.[15] Bergonzi et al., using synchrotron-based Fourier transform infrared (FTIR) microspectroscopy, showed the first clue that the water static properties were modified near a quartz boundary over a 1 $\mu$m thickness.[16] They speculated that the quartz surface of the pore walls was dominated by siloxane (hydrophobic) bridges, adding the long-range hydrophobic forces as an interfacial player. In a recent paper,[17] using three different and independent experimental setups, we confirmed the presence of such a micrometer-thick interfacial water layer near the surface of quartz.

We now aim to check whether this strikingly large interfacial layer may be related to idiosyncratic features of one peculiar inclusion or is ubiquitous, resulting from a specific surface field(s). To do that, we followed our previous methodology,[16,17] combining well-defined synthetic fluid inclusions (SFIs), a quartz-made analogue of "natural" pores, with the infrared energetic probe, measuring the vibrational energy that is prominent in the total internal energy of water. The interfacial layer was explored within cavities having three distinct geometries of inclusion, containing three different compositions of the occluded liquid, and finally along a 22−155 °C thermal ramp.

## 2. MATERIALS AND METHODS

**2.1. Synthetic Fluid Inclusions (SFIs).** Fluid inclusions are closed microcavities buried inside a crystal (i.e., typically quartz, calcite, fluorite, and barite) hosting liquid−vapor (sometimes even more complex) assemblages, with a constant composition and a nearly constant total volume.[18−20] Herein, SFIs were fabricated by hydrothermal protocols and filled with liquid water, either a dilute aqueous solution (~100 $\mu$M) of silicic acid, or impregnated with NaOH at different compositions.[21−23] The presence of NaOH buffers a very alkaline pH (~12.2) in water, which is the best means of promoting quartz solubility at room temperature (RT). Its addition therefore drastically improves the smoothness and the homogeneity of the inner surface walls.

Panels A−C of Figure 1 show the three SFIs with varied geometries (SFI-1−3) that contain liquid water at equilibrium with a bubble of saturated water vapor at RT. The second experiment tested three other inclusions containing different NaOH aqueous solutions at 0.5 M [SFI-4 (Figure 1D)], 1 M [SFI-5 (Figure 1E)], and 2 M [SFI-6 (Figure 1F)]. The third set of experiments subjected the largest and best-known SFI-1 (Figure 1A) to an increasing temperature, from RT to 155 °C.

**2.2. Mid-infrared Microspectroscopy.** High-resolution FTIR experiments were conducted at the Earth Sciences Institute of Orléans, ISTO (France). The state-of-the-art setup included a Continu$\mu$m microscope coupled to a Nicolet 6700 FTIR spectrometer featuring an XT-KBr beam splitter, both from Thermo Fisher Scientific (USA). The microscope was equipped with a liquid nitrogen-cooled mercury cadmium telluride (MCT) detector with a window of 50 $\mu$m, coupled with a 32× infinity-corrected Schwarzschild type objective (NA = 0.65; WD = 7 mm) and a 32× condenser. This system operated in the optical configuration known as "single aperture dual path mode", providing a confocal geometry in transmission mode.[16,17,24] With regard to the infrared source, we utilized the unpolarized supercontinuum laser (Coverage, Novae) operating in the mid-infrared range of 1.9−3.9 $\mu$m.[25,26] This laser was integrated with the spectrometer through an in-house-designed optical configuration (see ref 17 for more details).

In this configuration, an aperture size of 5 $\mu$m × 5 $\mu$m was reached with a high signal-to-noise ratio (SNR). The hyperspectral data (spectral linear and rectangular maps) of the SFIs were acquired with a 1 $\mu$m step size. Because the hosting quartz is opaque below 2000 cm$^{-1}$ and the supercontinuum laser source emits a continuous spectrum from 5260 to 2560 cm$^{-1}$, each FTIR spectrum was recorded in the spectral range of 2800−4200 cm$^{-1}$, with a spectral resolution of 8 cm$^{-1}$ and 256 scans. This spectral range corresponds to the OH stretching band of water, which is the adequate signature for following the H-bond networking in liquid water. It is known as the most sensitive band for characterizing the molecular environment of each molecule and its connectivity to the close neighbors, which feature the thermodynamic activity of liquid water. The background spectrum of the surrounding quartz matrix was recorded before each set of hyperspectral data to remove the effects of any changes in atmospheric $CO_2$ and water vapor. All of the acquired spectra were postprocessed, with baseline correction (by subtracting a linear baseline in the interval of 2800−4200 cm$^{-1}$), normalization with Origin Pro version 2021, and removal of interference fringes done by implementation of an algorithm in Igor Pro version 9.0 (see ref 17 for further details of data processing). A statistical treatment of the hyperspectral FTIR data was carried out through non-negative matrix factorization, implementing a script/algorithm in Python version 3.11.1, on the Jupyter Notebook platform.

**2.3. Thermal Study.** The high-resolution FTIR experiments as a function of temperature were performed by using the INS1402036 (INSEC) heating and cooling stage system. It comprised a stage, an mk1000 controller, and an LN2-SYS liquid nitrogen cooling device. This equipment allows one to work in a wide temperature range from −196 to 600 °C with a high accuracy of ±0.1 °C. The thermal ramps from 22 to 155 °C were performed at a rate of 10 °C/min associated with a time of equilibration of 60 min.


https://doi.org/10.1021/acs.langmuir.4c00742
Langmuir XXXX, XXX, XXX−XXX

The thermal range was chosen after a microthermometric analysis of our fluid inclusions, and Figure 2 exemplifies the procedure using

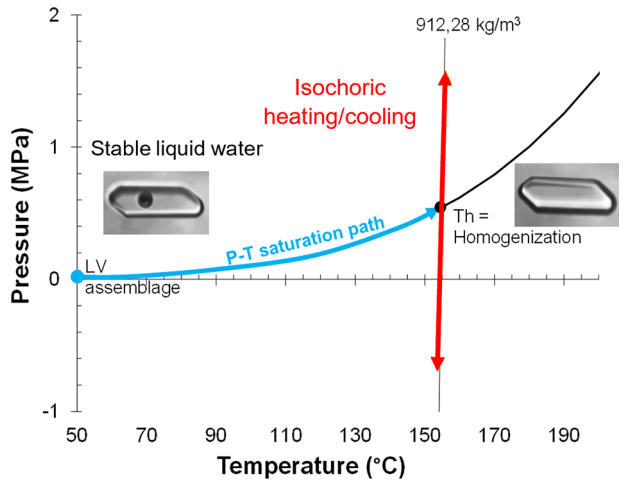


**Figure 2.** Phase diagram (calculated using ref 30) illustrated with the SFI-1 microthermometric measurements. The liquid water and bubble of saturated water vapor coexist along the water vapor saturation curve up to the homogenization temperature ($T_h$). SFI-1 displayed a repeatable (10 times) $T_h$ of 155 °C.

the data set obtained with SFI-1. Heating a liquid–air assemblage inside the closed cavity of a fluid inclusion has been used for decades as the most common way to delineate the phase diagrams of numerous systems of geochemical interest.[22] Setting the temperature imposes pressure (with or without quartz volume variation) on the fluid inclusion,[27] which forcibly follows the liquid–vapor saturation curve (blue curve in Figure 2). The size of the vapor bubble decreases with $T$, until reaching a special temperature where the molar volume of liquid under the $P-T$ conditions exactly fits the total volume of the cavity. This is the so-called temperature of homogenization, noted as $T_h$, obtained where the saturation curve crosses the characteristic isochore of the trapped liquid. It is a unique temperature at which the trapped fluid becomes single-phase (the fluid inclusion contains only water) (see refs 22 and 28 for further details).

Heating the monophasic liquid beyond $T_h$ increases the pressure along the steep isochoric curve (red curve in Figure 2). In that case, the $dP/dT$ Clapeyron slope is so large that pressure fluctuations put the SFI at risk of being damaged by what is known as decrepitation, namely the irreversible cracking of the quartz container.[29] It is why we did not exceed the $T_h$ value, recording the variations from RT to 155 °C. In what follows, the variation of the water pressure along that range (from 23 kPa to 0.54 MPa) will be considered negligible, and only the role of temperature will be discussed.

## 3. RESULTS

**3.1. Hyperspectral FTIR Data Set.** The inclusions were mapped to obtain a hyperspectral FTIR data set (i.e., $x-y$ distribution of IR absorbances). Using the microbeam provided by the supercontinuum laser setup,[17] it was possible to record how the OH stretching band profile changes, in terms of peak position (wavenumber, in inverse centimeters), peak intensity (corresponding to the absorption), full width at half-maximum (fwhm), or peak area, from one part of the inclusion to another, focusing here on the distance from each beam location to the solid walls.

It is now well established[16,17] that the water trapped in the middle of the inclusion displays spectral features similar to those of normal water, which is not the case for the water close to the water–solid interface that exhibits a distinct spectral profile. Consequently, water taken in the middle of the inclusion is called "bulk water", whereas approaching the cavity walls, water is labeled "interfacial water". According to previous studies,[16,17] interfacial water is systematically observed inside a micrometer-thick layer along the water–solid or water–air interfaces.

**3.2. Geometry of the Container.** On the basis of three different geometries (Figure 3), we verified whether the micrometer-thick layer observed in one inclusion depends on the geometrical dimensions of the container. The first inclusion displays a negative crystal shape [SFI-1 (Figure 3A)]; it is our sample of choice with which the chief previous results were acquired.[16,17] Its width (20 $\mu$m) and length (60 $\mu$m) are very large, separating the borders of the inclusion from its interior. Moreover, its thickness (5 $\mu$m) is commensurate to the wavelength, making it possible to observe specifically the top and bottom interface through the confocal geometry of our setup.[24] The water–solid interface is marked by a specific enrichment of the OH stretching band at high wavenumbers (Figure 3B), with a maximum absorbance shifted to ~3700 $cm^{-1}$ instead of the usual value of ~3400 $cm^{-1}$. The interface-marked band also becomes wider. The fwhm increases from 655 $cm^{-1}$ for the bulk to 751 $cm^{-1}$ for the interfacial water. This widening is accompanied by a blue-shift (band displaced toward higher wavenumbers) that is more visible on the low-wavenumber side of the band than on the high-wavenumber side (Figure 3A). Two $x-y$ spectral maps are drawn (Figure 3B), one showing the absorbance at 3400 $cm^{-1}$ ("bulk map") and another at 3700 $cm^{-1}$ ("interface map"). These maps make clear that the spectral interface-guided effect is visible over a regular constant thickness (~1 $\mu$m).

The second inclusion [SFI-2 (Figure 3C)] was chosen because of its rounder, smaller shape (~15 $\mu$m diameter), wherein a bubble is trapped, affording a continuous thick layer of water trapped between the bubble and the quartz walls. The FTIR map allows us to clearly distinguish the liquid water mass from the air bubble and displays the same spectral signature as the previous inclusion over a similar micrometer thickness (Figure 3D). Remarkably, we can record the layer sandwiched between bubble and quartz that is clearly interface-marked with the same spectral and thickness features seen for SFI-1 (Figure 3D).

The geometry of the third inclusion [SFI-3 (Figure 3E)] is still different with a tubular elongated shape, without any bubble in the recorded area of the FTIR map and therefore no water–air interface. Moreover, this inclusion shows a minimal wall–wall distance of 10 $\mu$m, making it possible to have one spot per interface and one for the middle place, combining the beam size and the step size. Here again, the regularity of the interfacial layer, in terms of both the spectral signature and the thickness, is remarkable irrespective of the proximity of the facing walls or the cylindrical geometry (Figure 3F).

According to Figure 3, both the representative spectra and the hyperspectral maps of the three SFIs show that the absorbance varies steeply from bulk type water far from the liquid–solid interface to a specific blue-shifted spectrum along the quartz boundaries, with a strong additional peak in the 3700 $cm^{-1}$ region. In our previous publication,[17] we demonstrated that the transition between the two regimes appears sharply (at the beam size resolution) ~1 ± 0.5 $\mu$m from the solid boundary. Importantly, the findings presented in this study affirm that the IR-based thickness of interfacial water remains almost constant across the cavity shapes and dimensions. This indicates that the underlying interface-driven


https://doi.org/10.1021/acs.langmuir.4c00742
Langmuir XXXX, XXX, XXX–XXX

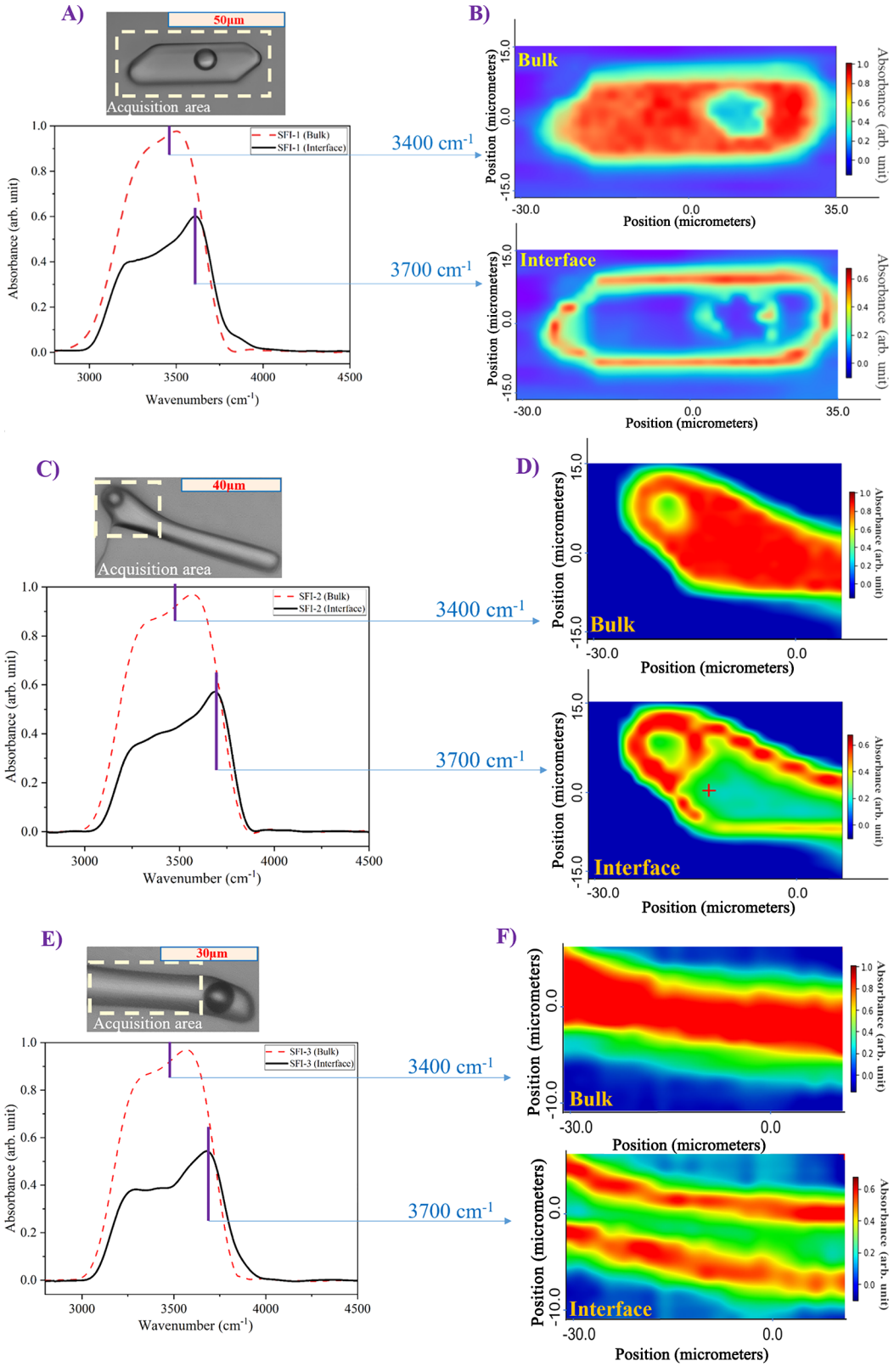


**Figure 3.** Representative/average FTIR spectra of the bulk and interface in (A) SFI-1, (C) SFI-2, and (E) SFI-3. Absorbance distribution maps of (B) SFI-1, (D) SFI-2, and (F) SFI-3 with regard to the two characteristic wavenumbers correspond to the bulk (featuring the 3400 $cm^{-1}$ peak) and interface (featuring the 3700 $cm^{-1}$ peak).

factor(s) contributing to this effect is independent of the pore's shape or dimensions.

**3.3. Composition of the Occluded Solution.** Changing the composition of the occluded liquid in the fluid inclusion is another important feature that can modify the spectral signature of water. As interfaces modify the ionic distribution (double-layer effect[31−33]), we might consider that our IR data sets reflect a changing composition. To enhance the effect, we



https://doi.org/10.1021/acs.langmuir.4c00742
Langmuir XXXX, XXX, XXX−XXX

utilized a NaOH-bearing solution ranging in concentration from 0.5 to 2 M. This solution significantly amplifies the solubility of quartz, increasing it from 150 μmol/kgw at pH 6.8 when absent (SFI-1−SFI-3) to 0.43 M $Si_{total}$ at pH 12.2 (SFI-4, 0.5 M NaOH), 0.9 M $Si_{total}$ at pH 12.15 (SFI-5, 1 M NaOH), and 1.87 M $Si_{total}$ at pH 12.15 (SFI-6, 2 M NaOH). These molal concentrations have been calculated using the Pitzer-based model implemented in the PhreeSCALE software adapted to a high ionic strength and including the polymeric silica-dissolved species.[34−36] The dissolved silica is mainly anionic at these pHs, buffering the pH with respect to the increasing amount of the Na cation. Figure 4 reports the

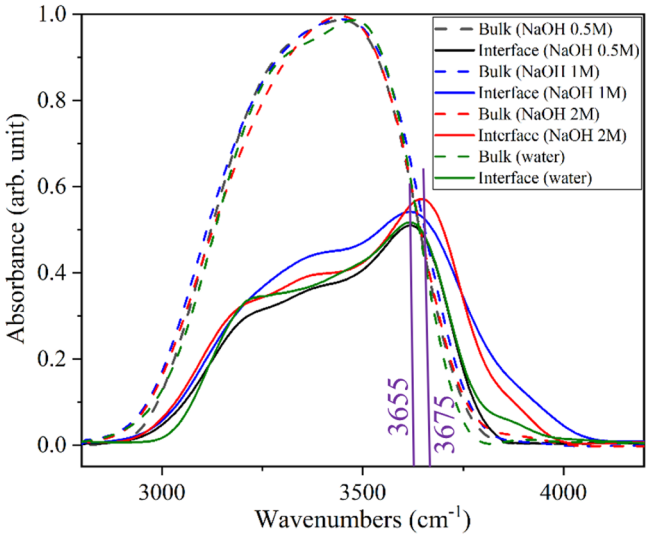


**Figure 4.** Micro-FTIR spectra of water and a NaOH solution with different concentrations in the bulk (dashed line) and near the solid−liquid interface (solid line).

micro-FTIR spectra of NaOH solutions taken either in the middle of the inclusion or along the water−solid interfaces. The bulk data set shows no significant differences with respect to the very dilute water recorded in the previous inclusions (i.e., SFI-1−SFI-3) regardless of their NaOH and $Si_{total}$ concentrations.

The "interface" spectral data set displays similar features as before, with a blue-shift and a band widening, making clear that the composition is not responsible for the main features of the interfacial signature. In detail, increasing the concentration causes a slight variation with higher absorption values of the main peaks and a blue-shifted behavior by ∼20 $cm^{-1}$ per mole of NaOH. These features are of secondary significance with respect to the strong impact of the interface and therefore establish that the interfacial signature cannot be related to a composition-guided driving force. They also outline the sensitivity of the micro-FTIR probe to record how the water rearranges along interfaces.

The three NaOH-bearing inclusions are small and have varied geometries. More precisely, SFI-4 and SFI-5 are everywhere larger than one beam spot, and the linear maps display the now-usual feature, with a sequence of interface-marked signatures followed by bulk spectra (Figure 5A,B). SFI-6 (Figure 5C) shows a peculiarly interesting linear map. Herein, the distance from one wall to the other is limited to 4 μm, while the beam is 5 μm. Moving the beam from the quartz container to the inclusion allowed us to obtain the interfacial "usual" signal, which disappeared when the beam crossed a large amount of in-cavity water. This means that the beam cannot record the interfaces when they are diluted by a large amount of bulk water, even if it is certain that part of the beam is crossing the water−solid interface. The interfacial signature can be recorded only when moving the beam from the quartz crystal and entering very progressively inside the cavity (step size of 1 μm), to illuminate only (or mainly) the interfacial zone. When moving from the edge to the center of the cavity, the IR beam encompasses progressively more and more of the bulk water and proportionally less and less of the interface. There is therefore a possible dilution of the interfacial signature once the beam is involved in the bulk compartment.

Consequently, we confirmed with this data set that the geometry of the water-bearing cavity does not affect the scope of the interfacial signature or the composition.

This relative insensitivity of interfacial water to pH can be confronted with SFG measurement, which displayed a strong pH-guided spectral variation of water deposited on hydrophilic materials.[37,38] The very classic interpretation refers to the modification of the surface charge of silica with pH that determines a modification of the connectivity of the hydrogen bonds between surface water and the solid surface. With hydrophilic materials, as the pH increases, the connectivity increases, and the band promotes the absorbance at small wavenumbers. With our hydrophobic quartz walls,[16] the water spectra barely change from pH 6.8 to 12.2, which gives strong grounds that the connectivity between $H_2O$ molecules and the quartz surface is very low, related to the hydrophobicity of the surface. Many experiments (e.g., refs 39−43) and theoretical simulations (e.g., refs 44−46) detected a layer of small nanobubbles along hydrophobic walls, or alternatively a water layer at a very low density, which characterizes the absence of, or the very low, connectivity between the extended hydrophobic surface and water.

Finally, we recorded a hyperspectral map on the smallest round inclusion (i.e., SFI-5). Figure 6 shows the yet-classical scheme with the interfacial layer developed all around the solid walls.

**3.4. Effect of Temperature.** A subsequent temperature-dependent study intended to disturb the interfacial signature by providing a significant amount of external energy. The key target is to record how the interface signature behaves against a strong energetic perturbation. The thermodynamic significance of the temperature-dependent signatures is also of great interest for deciphering the underlying driving force, particularly in the context of enthalpy−entropy compensation.

In terms of procedure, a series of FTIR measurements were recorded by increasing temperature from RT (22 °C) to $T_h$ (155 °C), differentiating the middle part of the inclusion from the wall area (Figure 7). The profile of the spectra (i.e., main peak position, band shape, and absorbance values) exhibits *T*-dependent variations while maintaining the constancy of the key features that distinguish a bulk spectrum (in the middle) from an interfacial one (at the edge). The spectral behavior of water is marked by a blue-shift with an increase in temperature as expected,[47−58] for both the bulk and the interfacial regions (rear arrows in Figure 7). The most remarkable fact is the observation that the interfacial signature is constantly present throughout the thermal ramp and is blue-shifted by *T* as the bulk. This observation is definite proof that the interface signature is not a local artifact and is related to a


https://doi.org/10.1021/acs.langmuir.4c00742
Langmuir XXXX, XXX, XXX−XXX

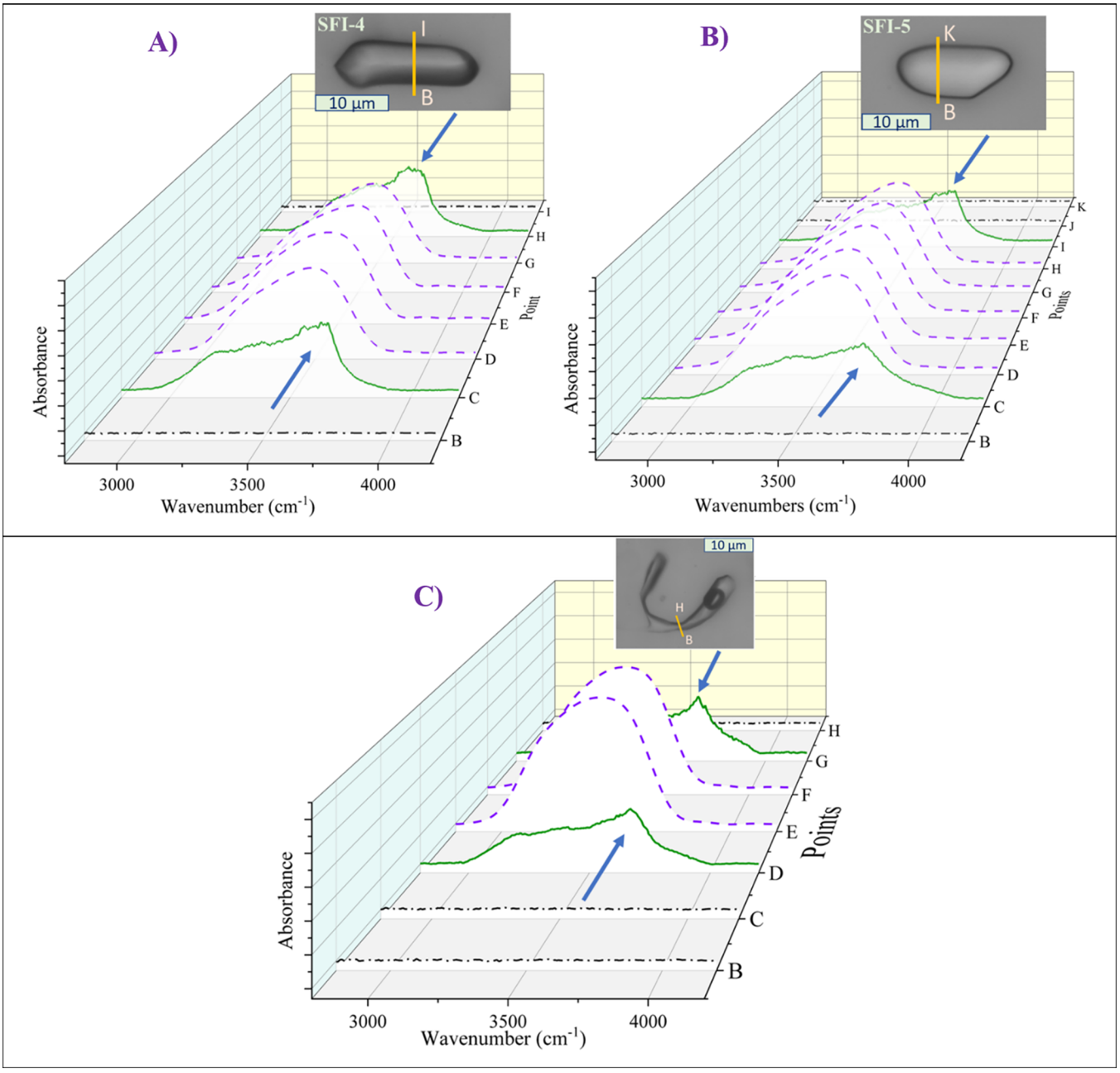


**Figure 5.** Variation of the OH stretching band recorded across the (A) SFI-4 (0.5 M NaOH) (from point B to I), (B) SFI-5 (1 M NaOH) (from point B to point K), and SFI-6 (2 M NaOH) in a narrower scope (4 $\mu$m length, from point B to point H). Black lines (dashed−dotted line) correspond to quartz, green lines (solid line) to the near liquid−solid interface, and purple lines (dashed line) to bulk behavior.

thermodynamic field force that is itself sensitive to the physical conditions.

The SNR, however, decreased during the measurements between 105 and 130 °C (Figure 7), due to the shrinking of the trapped bubble with $T$. Because the size of the bubble decreases, the wall-to-wall adhesion is lost and the bubble starts moving freely inside the cavity, intercepting the beam from place to place and even following it. Consequently, the bubble spectrum overlays the liquid water spectrum, leading to a decrease in the SNR and a deformation of the final spectra.

The blue-shift with $T$ can be closely examined by looking at the isosbestic point. This point represents the wavenumber at which all absorption curves acquired at different temperatures intersect, exhibiting identical wavenumber and absorbance values. Certain authors remarked that the isosbestic point can slightly migrate with $T$, which is why they prefer to call it a quasi-isosbestic point.[47] This crossing point is commonly linked to an equilibrium between the H-bonded and non-H-bonded water molecules[48,57,59,60] or between molecules engaged in extended connective networks and those outside these networks.[47] This two-state scenario requires H-bonds being formed and broken in a collective mode, a proposition against which many authors are strongly advocating (e.g., ref 61) because it may involve the existence of localized "clusters" congregating some $H_2O$ molecules in two specific ways. In Geissler's viewpoint, the isosbestic point is assigned to the inhomogeneous broadening of the stretching band with $T$ without any link to two molecular populations.[61] Maréchal[51,62]


https://doi.org/10.1021/acs.langmuir.4c00742
Langmuir XXXX, XXX, XXX−XXX

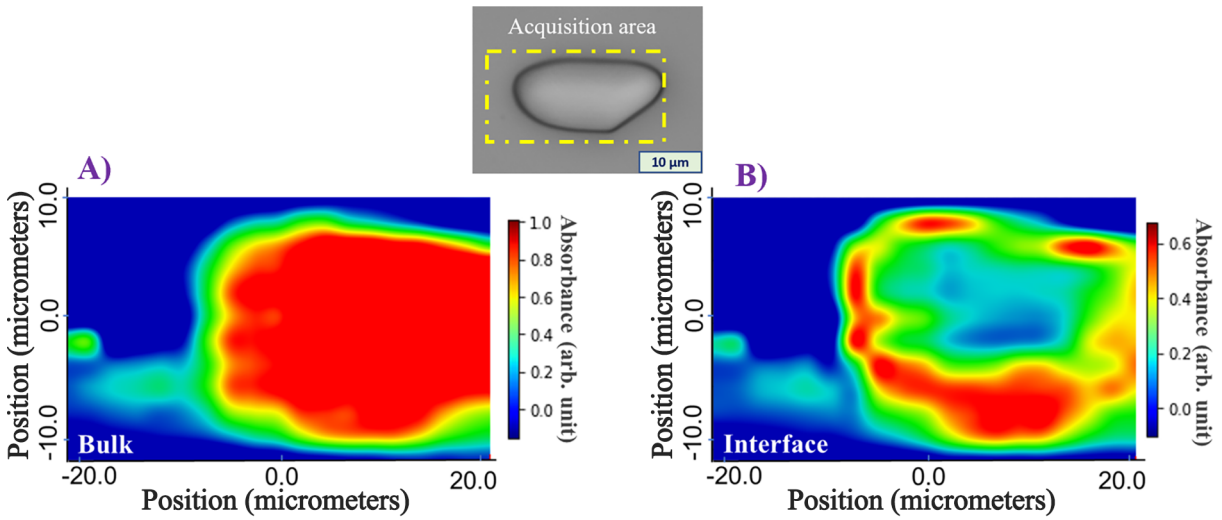


**Figure 6.** Absorbance distribution maps of SFI-5 (1 M NaOH), regarding the two characteristic wavenumbers, correspond to the (A) bulk (at 3400 $cm^{-1}$) and (B) interface (at 3700 $cm^{-1}$).

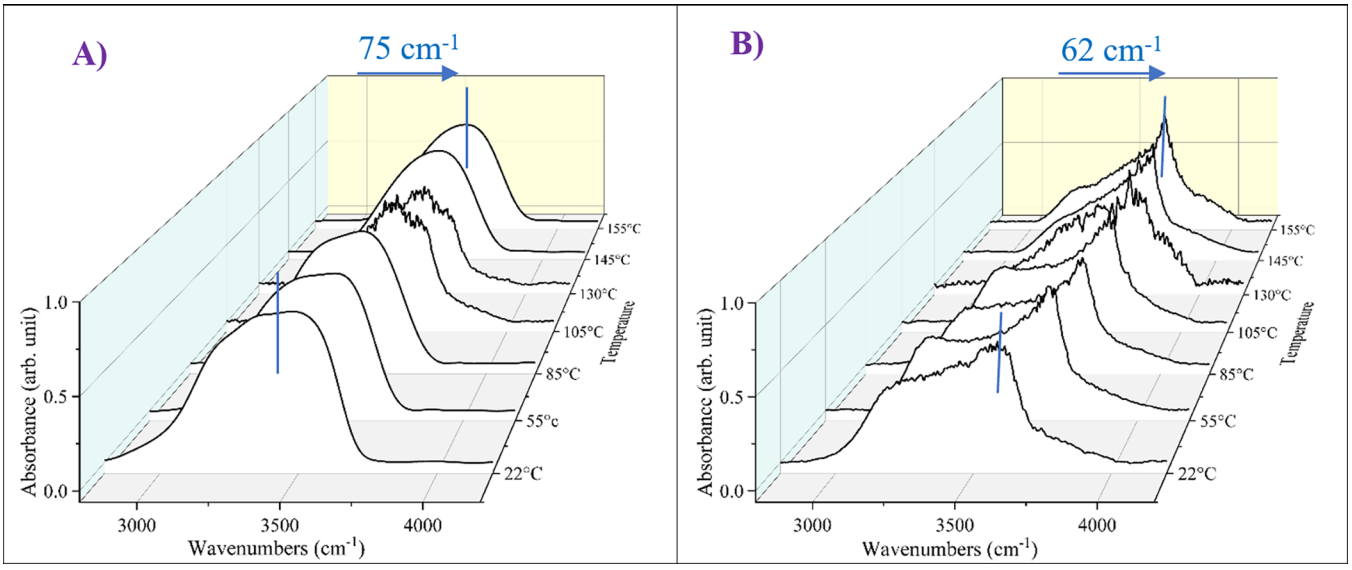


**Figure 7.** Average/representative spectral variation of SFI-1 at seven different temperatures (from RT to $T_h$) in the (A) bulk and (B) interface.

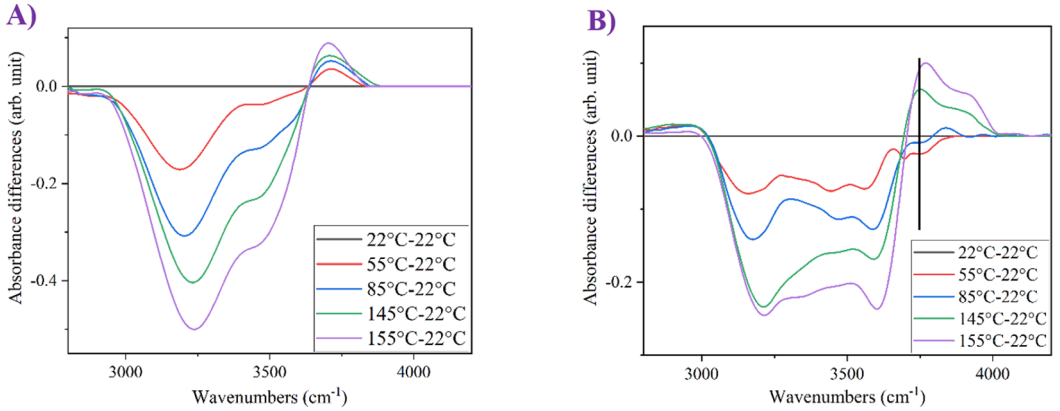


**Figure 8.** FTIR absorption spectra depicting OH stretching bands in (A) bulk water and (B) interfacial water, obtained from the differences between the spectra at various temperatures ($T$) and room temperature (RT).

outlined that the continuous picture is not at all exclusive of the existence of two types of $H_2O$ molecules, if looking at the complete spectrum of water and not only at the intramolecular stretching band (as done by Geissler). In these two papers,


https://doi.org/10.1021/acs.langmuir.4c00742
Langmuir XXXX, XXX, XXX−XXX

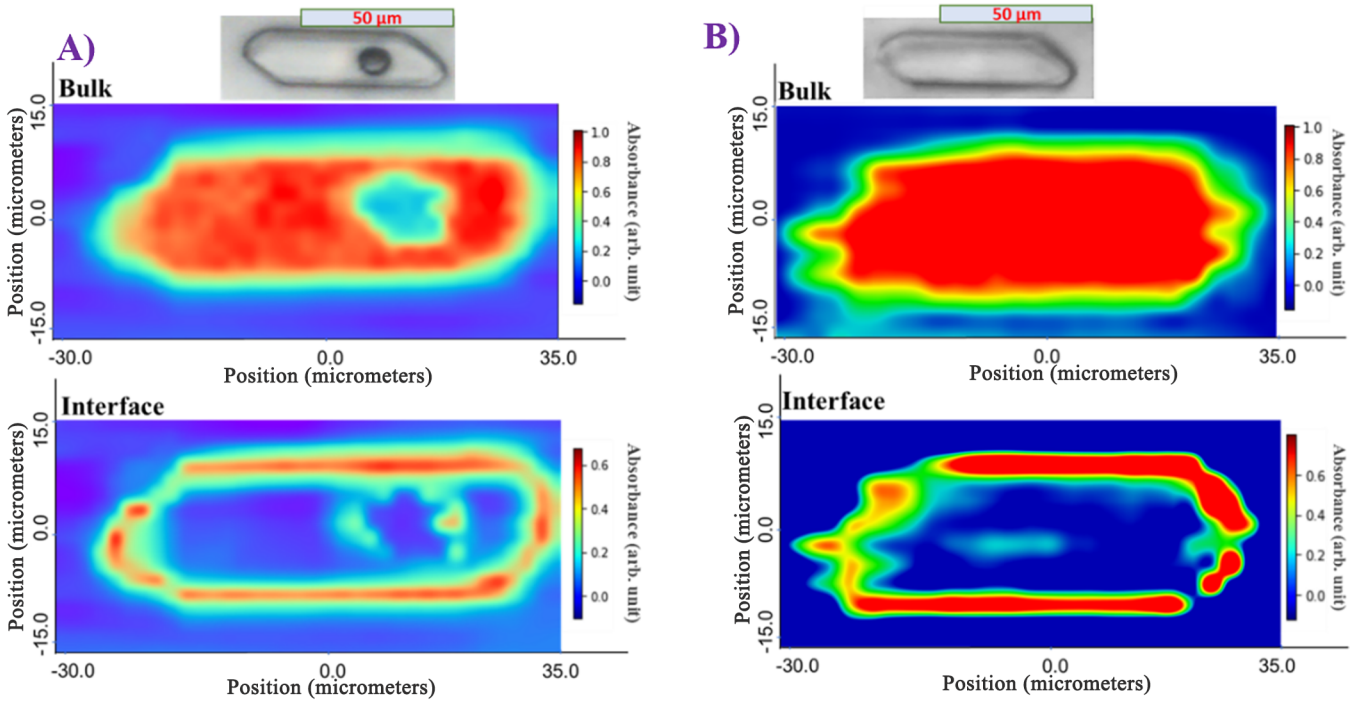


**Figure 9.** Hyperspectral maps of SFI-1 acquired at (A) 22 and (B) 155 °C showing the distribution of absorbance at two characteristic wavenumbers: 3400 $cm^{-1}$, which relates to the bulk, and 3700 $cm^{-1}$, which represents the interface water behavior.

Maréchal demonstrated the coexistence of two types of water molecules: one in its fundamental state and one in its first excited librational state. The latter retains greater rotational amplitudes and therefore displays a shorter relaxation time. In this conceptualization, the presence of two populations is replaced by the presence of two types of $H_2O$ molecules, statistically distributed in the water network, but of varying proportion as a function of external constraints, for instance, $T$ (see especially ref 62). The observation of an isosbestic point becomes compatible with a continuous distribution of H-bonds of various energies that rapidly interchange due to the great amplitude libration of molecules, but according to two time scales due to the two librational features. Moreover, the $T$-driven band broadening of the stretching band was recognized[51] as an effect of H-bonded systems, again attributed to couplings of intramolecular vibrations with intermolecular modes, typically the couplings between the OH stretching and the librations.

The wavenumbers of the isosbestic point for liquid water in the range of 0−100 °C have been reported to be 3460 $cm^{-1}$,[50,59] 3480 $cm^{-1}$,[47,51] and 3550 $cm^{-1}$.[62] The position of the isosbestic point in the middle of the inclusion (i.e., bulk water) is here measured at 3614 $cm^{-1}$ and shows no shift with $T$ (Figure 8A). This means that bulk water retains a "true" isosbestic point that is located at wavenumbers higher than the previously published position. This adds new evidence that the in-cavity water is slightly band-broadened with respect to "normal" water, especially toward higher wavenumbers as recently concluded.[17] The interfacial water does not display a clear isosbestic point (Figure 8B), especially with the intermediate $T$ values, 55 and 85 °C, the blue-shift of which is similar to that of RT. Only reaching the highest $T$ seems to "restore" the isosbestic behavior. Unfortunately, 105 and 130 °C had to be discarded because of the spectral deformations induced by the superimposition of the air bubble during the measurements (Figure 7A,B). For the two highest $T$ values, 145 and 155 °C, the isosbestic point slightly migrates with $T$ and behaves as a quasi-isosbestic point[47] at 3658 $cm^{-1}$, therefore at a value still larger than that of the bulk. This very specific behavior once again outlines that within a large interface region water is significantly modified from the bulk. Moreover, this $T$-dependent eclipse of the isosbestic behavior is puzzling, especially considering that both the interface and $T$ have a blue-shifting influence. The absence of any isosbestic point up to at least 85 °C indicates that the influence of $T$ is overcome along that $T$ range by the interfacial field that froze the water reorganization in a new state that is not significantly affected by the change in $T$. When $T$ reaches a certain threshold between 85 and 145 °C, the impact of $T$ can predominate over the interfacial one, restoring therefore the isosbestic $T$-based behavior.

Finally, we compared the absorbance distribution maps of SFI-1 at 22 and 155 °C (Figure 9). A direct comparison of the hyperspectral maps between the two extreme temperatures (RT and $T_h$) reveals two major features. (i) The thickness of the interface-driven effect, i.e., the distance over which the interface signature is detected, remained almost constant, possibly slightly increasing. (ii) The intensity of the surface-imprinted signature increases with $T$, resulting in a more marked surface water layer at high temperatures.

## 4. DISCUSSION

**4.1. Statistical Analysis of the Hyperspectral Maps.** Non-negative matrix factorization (NMF) is a statistical treatment employed to reduce the dimensionality of the data sets and increase interpretability while preserving the maximum information based on the multivariant analysis of the hyperspectral data.[63−65] NMF decomposes a data set matrix into its two non-negative matrices whose dimensionality is uneven and chooses the best factorization rank and the


https://doi.org/10.1021/acs.langmuir.4c00742
Langmuir XXXX, XXX, XXX−XXX

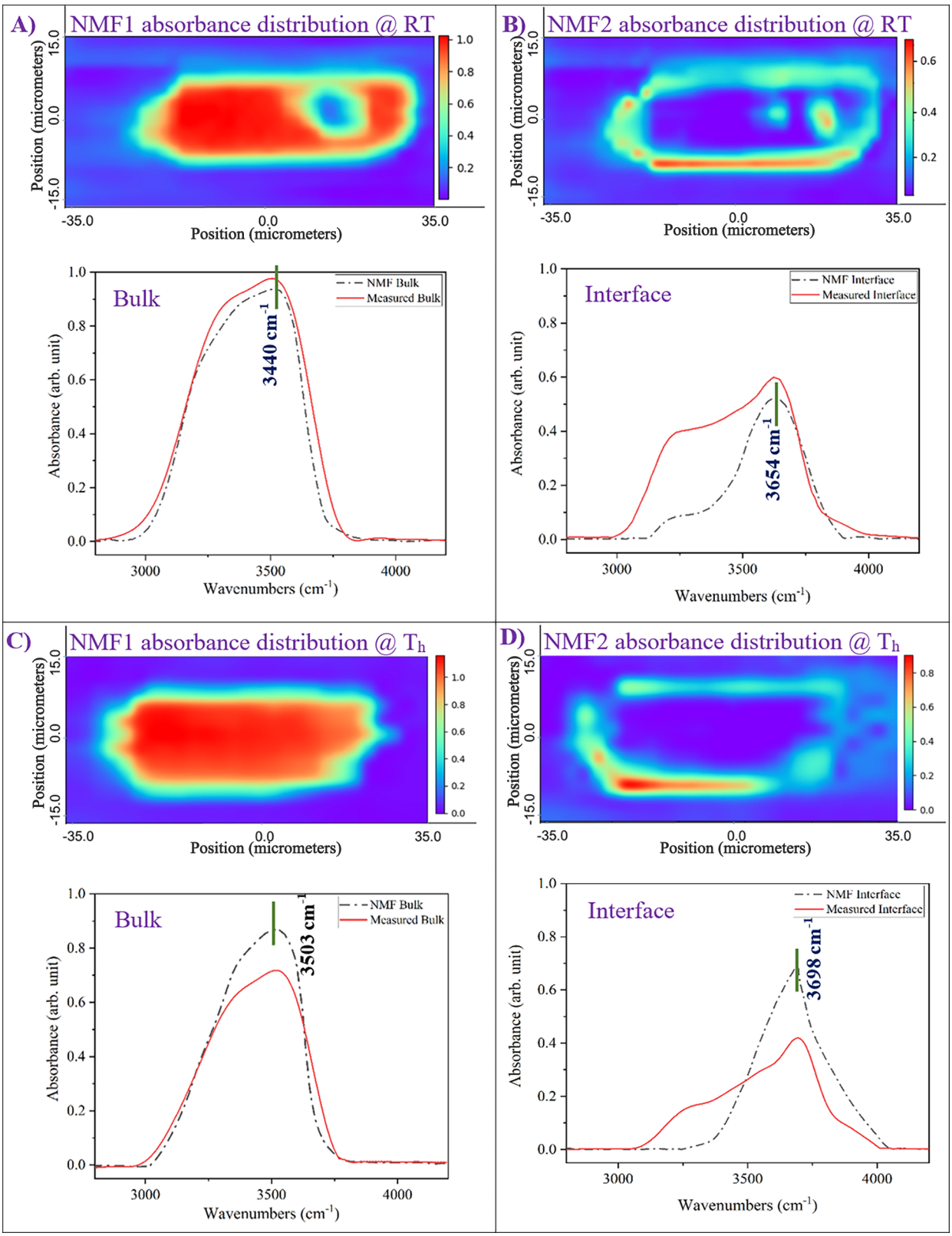


**Figure 10.** Non-negative matrix factorization (NMF) analysis of FTIR hyperspectral maps. NMF1 at (A) RT and (C) $T_h$ and NMF2 at (B) RT and (D) $T_h$ compared to their representative/average measured spectra.

number of components that are meaningful to the analysis. In NMF, one matrix represents the spectral signatures indicating different components (often termed "scores" or "basis vectors"), and the other expresses the information about the presence and contribution of these components (also known as "loadings" or "coefficients").[66,67]

In our Python script, the function was designed to provide a comprehensive visualization by plotting the components



https://doi.org/10.1021/acs.langmuir.4c00742
Langmuir XXXX, XXX, XXX−XXX

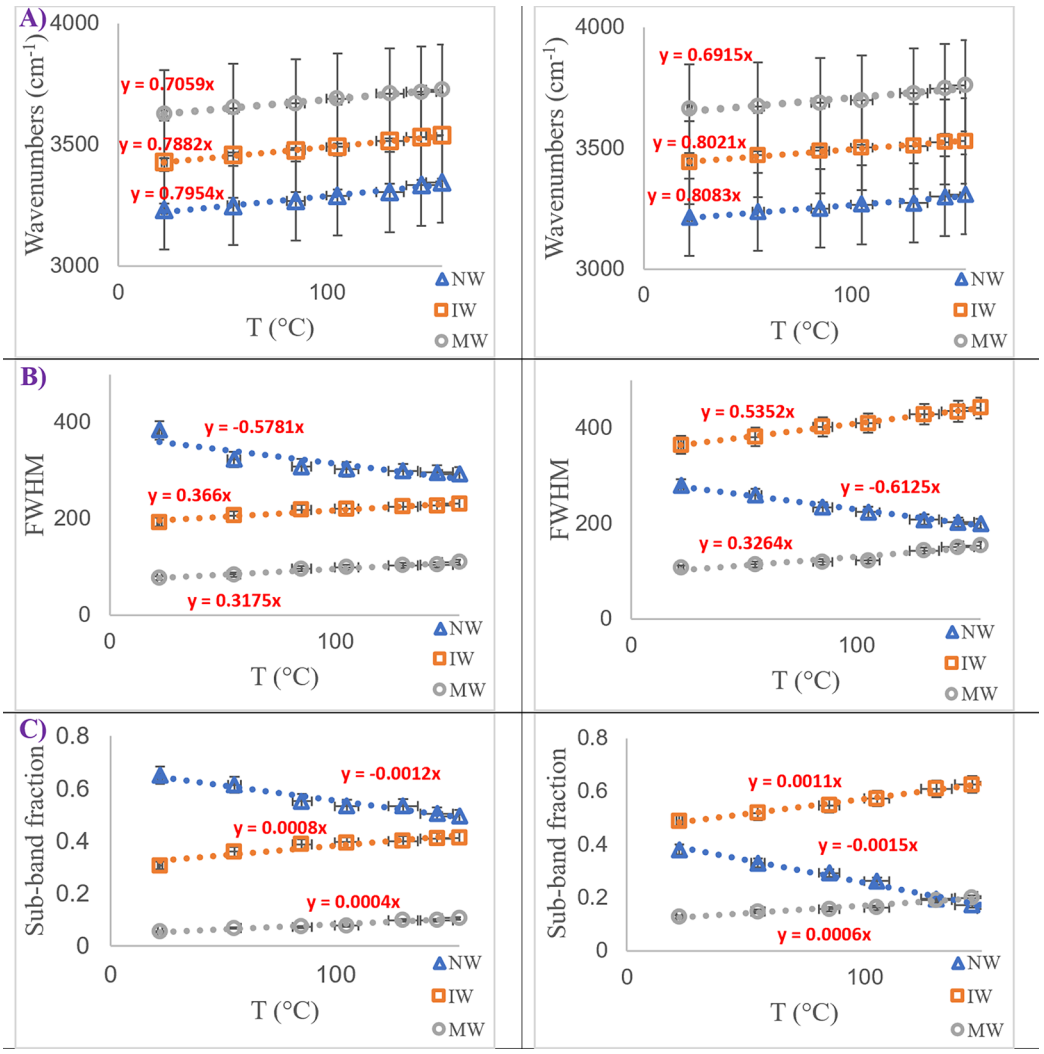


**Figure 11.** Main peak parameters, such as (A) peak position, (B) fwhm, and (C) sub-band fraction (contribution of each sub-band) in the bulk (left) and interface (near the quartz boundary) (right) at different temperatures.

alongside their corresponding map representations, illustrating the distribution of each component across the entire map. The input spectra typically consist of the matrix detailing the contributions of components within each spectrum, capturing the variations across the data set. Meanwhile, the array of scores will encompass the distinct components under analysis, facilitating a clear understanding of their individual impact within the data set. This combined visualization approach offers valuable insights into the spatial distribution and relative importance of each component, enhancing the interpretability of the results of the analysis.

Figure 10 shows the scores and loadings of that analysis as a function of the IR beam location in the inclusion at the two characteristic temperatures, RT and $T_h$. NMF analysis affords two components. The first component (NMF1) is almost equivalent to the measured spectrum of bulk water at the two $T$ values (Figure 10A,B). The second component (NMF2) reveals a spectrum that is deeply different from that of the bulk but also different from the interfacial data set. The additional peak at ~3700 $cm^{-1}$ appears and predominates, as was already concluded from measurements at the two $T$ values, but an important lack of contribution from the low-wavenumber region of the band characterizes this NMF2. It is obvious that the mean coordination of the water molecules located close to the quartz wall clearly decreases. The two NMF components correspond to the two "extreme" behaviors that can be extracted from the statistical diversity of the data sets, without any external constraints to guide the NMF toward a specific spectral profile. Interestingly, the loadings are 56.87% for NMF1, 9.95% for NMF2, and 33.18% for quartz (normalization to 100%), leading to the conclusion that the respective behaviors are neatly marked in the data set. The NMF2 score shows a spectrum that differs from that of the bulk but also from the mean measured spectrum along the interfaces. NMF analysis maximizes the difference but is basically linked to the data sets, so each score is the extreme value that can be extracted from the total extent of spectra existing in the data set. It is consequently possible that the "true" interface signal would not be the one we have measured but something still different, closer to NMF2. This analysis does suggest that the interfacial signature is at a still smaller scale than our combination of the beam probe and beam size delineates. What we are calling the interfacial layer over 1 $\mu$m may be a convolution of water involved in a thinner interface with bulk water.

The influence of the interface signature is retrieved here as a blue-shift, consistent with the raw data. Specifically, the bulk-to-interface shift of the main peak is 214 $cm^{-1}$ at RT and 195


https://doi.org/10.1021/acs.langmuir.4c00742
Langmuir XXXX, XXX, XXX−XXX

$cm^{-1}$ at $T_h$ (9% variation), evidencing that (i) the interface field is energetically expensive (~2.5 kJ/mol after the main peak variation) and (ii) the interface takes place at a pretty similar cost regardless of the $T$. Additionally, the $T$-dependent shifts of the main peak are 63 $cm^{-1}$ for the bulk from RT to $T_h$ and 44 $cm^{-1}$ for the interface over the same range, which can be considered as a similar variation. These two remarks are consistent with what was concluded from the raw data in the $T$-dependent study (section 3.4).

The most interesting observation is that the interface signature is much different from the bulk, probably at a scale thinner than that of the probe. As a result, all of the data sets are prone to being interpreted with a simple core−shell model, as promoted previously for water trapped in hydrophilic 8−320 nm pores.[11] Of course, their observations were exactly the opposite (i.e., enrichment of low-wavenumber components of the OH stretching band of water), due to the hydrophilicity of the substrate and the role of confinement. In our ultralarge pores, no confinement effect can be expected, so that the pore size has no impact, and the walls are hydrophobic as described previously.[16,17] The basic idea is that the interface spectral signature is large enough to imprint the IR band as long as the volume ratio of the surface layer versus the bulk domain "seen" by the microbeam would be "sufficient" (no number here). From that viewpoint, the band broadening of what we call "bulk water" in this paper with respect to normal water[17] would be a remnant signature of this convolution. Even in the middle of a large inclusion, the 5 $\mu$m microbeam forcibly crosses the top and bottom quartz−water interfaces. As the spectral plane of the beam (wavelength varies from 3.33 to 2.63 $\mu$m along the stretching band) is commensurate with the thickness of the inclusion (5 $\mu$m), all measurements contain a certain fraction of an interfacial signature. At present, the quest is toward reducing the beam size, possibly using submicrometer IR imaging, to obtain experimental measurements of this "true" interface signal.

**4.2. Decomposition of the FTIR Spectra.** To go further, we decomposed the OH stretching band into three Gaussian sub-bands,[11,47,68−71] each directed toward a specific population of probed molecules defined by the number of close neighbors (i.e., degree of connectivity or H-bond coordination number).[69,72−76] The decomposition was done using the peak analyzer function tool of OriginPro version 2021, and a least-squares regression value of >0.993 allows the validation of the chosen models. The regression is carried out with the wavenumber of each sub-band let free inside a spectral range: 3150−3350, 3351−3550, and 3551−3750 $cm^{-1}$ for the first, second, and third sub-bands, respectively. Meanwhile, the fwhm and integrated surface area parameters were left free.

The first low-wavenumber component (3231 ± 34 $cm^{-1}$) is related to the strongly H-bonded water molecule [network water (NW)] having a coordination number close to four. The second component with an intermediate wavenumber (3429 ± 21 $cm^{-1}$) corresponds to water molecules with a coordination number from two to three, called intermediate water (IW). The last one (high wavenumber, 3628 ± 36 $cm^{-1}$) can be assigned to the less connected water molecule with a small number of H-bonds (one to zero); they are considered multimer water (MW).[11,16,47] The sub-band contribution (sub-band fraction) to the water spectra can be easily calculated as the ratio between the integrated area of each sub-band ($A_{iW}$) to the total integrated area ($\sum A_{iW}$).

Accordingly, the temperature evolution of the peak position (wavenumbers, inverse centimeters), the fwhm, and the sub-band contribution to the total band are plotted in Figure 11 for bulk and interfacial water. At RT, the comparison of bulk and interfacial water reveals that the interfacial water is predominantly influenced by the IW fraction over the NW fraction (Figure 11C), whereas classically the predominance of the NW is one of the main infrared features of liquid water. This implies that water molecules exhibit a reduced degree of average self-networking when approaching the solid walls. We are quantifying the change by plotting the NW/IW ratio, which is 2.16 for bulk water and decreases significantly to 0.77 along interfaces. This fact points to the reduced activity of tetrahedrally connected molecules together with an increasing activity of less connected molecules, which requires a mean breaking of H-bonds from the bulk to the interface, corresponding to an enthalpic penalty. The fwhm of interfacial water (Figure 11B) is also atypical with a larger value for the IW sub-band than for the NW sub-band. It is another clue for the same conclusion: the IW population becomes predominant along the interface over the NW population, which usually occupies the widest spectral surface and constitutes the larger fraction in liquid water.

The $T$-dependent evolution in Figure 11 is also interesting, as evidenced by the slopes of the curves. All considered parameters for the three sub-bands display similar slopes of variation with $T$ among interfacial and bulk water, but these $T$ slopes are systematically slightly larger for the interfacial behavior. Only the wavenumbers of MW with $T$ along the interface are the exception, showing a (limited) decreased sensitivity to $T$ compared to that of its bulk counterpart, to the benefit of the IW band.

We can detail this similarity of the $T$ dependence between the two domains. The general blue-shift of the main peaks of the three sub-bands for the bulk and interfacial water (Figure 11A) demonstrates a connectivity loss with an increase in $T$ as liquid water becomes more volatile. The band intensity also decreases for water within the two domains, a common observable when liquid is heated.[57] The fwhm of the two types of waters (Figure 11B) exhibits a decreasing pattern for NW and an increasing trend for IW and MW, indicating the reduced activity of tetrahedrally connected molecules as the temperature increases, to profit from the two other contributions, especially the IW that increases the most. The fraction of each sub-band (Figure 11C) reveals a substantial decrease in the NW fraction with an increase in temperature, while the other two fractions experience an upward trajectory. As a whole, the three parameters examined with $T$ make it clear that the temperature promotes a certain degree of H-bond breaking in the $H_2O$ network, which is quite consistent with the decreasing latent heat of vaporization.

Then, we can discuss how interfacial water deviates from bulk behavior. Along the interface, each sub-band shifts toward higher wavenumbers with $T$ like those of the bulk, but either more than those of the bulk (IW and NW) or less than those of the bulk (MW) (Figure 11A). The IW peak shift with $T$ explains most of the general peak variation through $T$, demonstrating that it represents the population most relevant to characterization of the interface behavior. In terms of fwhm, the IW sub-band of interfacial water at RT neatly overcomes its NW counterpart, making it clear that the contribution of these IW populations strongly controls the average percolation of H-bonds. As $T$ increases, both sub-bands, namely, IW and NW,


https://doi.org/10.1021/acs.langmuir.4c00742
Langmuir XXXX, XXX, XXX−XXX

exhibit patterns similar to those observed in the bulk, where there is a positive slope for IW and a negative one for NW. However, there is a intensification of the noticeable gap between them. This occurs because the fwhm of the NW decreases, whereas the fwhm of the IW increases more than that of the bulk (Figure 11B). At 155 °C, the sum of two fwhm's of NW and MW in bulk covers together only half of the fwhm of IW in the interface. The decreasing coordination number of water molecules along the quartz boundary is therefore enhanced with an increase in $T$ more than the trend shown by bulk water. In molecular terms, this situation corresponds to an increasing distance between neighbor molecules and a varying length of the O−H···H bond.[71] Averaging that fact over a large number of molecules means that the average intramolecular force decreases, leading to the fading of the H-bond of each molecule established with its possible neighbors. Again, this conclusion is in line with the enthalpic cost of the interfacial reorganization, because it means a diminishing average potential energy of interaction between molecules.[77] The sub-band fraction also exhibits interesting trends. As $T$ increases, there is a convergence between NW and MW, each representing 20% of the total population at 155 °C, while IW predominates (60% of the total). This represents a significant distinction from bulk water, where the populations of NW and IW are both slightly <50% each at 155 °C, even though NW still holds a predominant position. As a consequence, the most significant feature of water involved in the interfacial layer is a chaotropic (IW predominance) effect sensitive over almost 10 000 water "monolayers". This observable forcibly corresponds to both an enthalpic penalty, namely an average disruption of H-bonds from bulk to interface, and an entropic driving force, echoing a decreasing degree of order of the intermolecular correlations.[77] This chaotropic effect is either constant or possibly slightly enforced with $T$, according to the (modestly) increasing $T$ slopes of the various parameters when coming closer to the quartz walls (Figure 11). The interfacial water appears thus enthalpically penalized, entropically promoted, and globally chaotropized, making it slightly more sensitive to the thermal supply than the bulk. In other words, the lower average molecular connectivity of interface water enhances its sensitivity to the heat supply, namely, decreases the heat capacity of water along the interface. However, this conclusion is at odds with what we inferred from the NMF features, where the interface seemed more independent of $T$ than bulk water. Obviously, any definite conclusion about that precise point is blurred by conceptualizing the interface region. On the basis of the results obtained from NMF, it appears that a core−shell model could potentially align with the data. At this stage, we cannot proceed without more spatially resolved data sets.

All of these FTIR measurements and their decomposition can be usefully compared with results obtained from water confined in nanoporous hydrophilic silica materials. These systems have opposite wall wettability (i.e., solid surface chemistry), and interestingly, they exhibit opposite trends. Water on hydrophilic silica displayed a decreasing density and surface tension,[71,78] an increasing heat capacity,[79] and a red-shift of the OH stretching band with an increase in NW and a decrease in IW.[11] In this last very complete study,[11] the authors postulated that the red-shift comes from a surface shell of water molecules superimposed to the normal behavior expressed in the rest of the nanopore (from 8 to 320 nm), a core−shell model of in-pore water. They determined that this surface layer varies with pore size from 3 to 30 nm. The silanol surface groups, characteristic of hydrophilic materials, are assumed to play a major role in that confinement effect, congregating highly coordinated water molecules.[11]

This simple comparison, revealing analogous yet opposing trends during the transition from interface-free to interface-driven signatures, prompts the conclusion that hydrophobic forces play a pivotal role. These forces disrupt water hydrogen bonding, leading to a reduction in cooperativity, an increase in entropy (indicative of order loss), and an increased enthalpy due to the cleavage of hydrogen bonds. Consequently, the emergence of interfacial water can be attributed to a chaotropic effect, in particular, the loosening of hydrogen bonds. This effect is intricately linked to the diminished cooperativity of water close to the hydrophobic pore walls. Finally, it is worth mentioning that the link between the two surface-driven situations remains debatable, with no confinement in our ultralarge (in terms of confinement threshold) liquid-bearing cavity, compared to the confinement possibly arising in nanopores.

In conclusion, two synergistic effects played a role in forming the IR signatures of the in-cavity water: (1) the thermal effect and (2) the interface-driven effect. The geometry of the container and the composition of the occluded liquid did not imprint the IR spectra, at least commensurably to $T$ and solid walls. The proximity of the hydrophobic solid boundary, with an increase in $T$, results in a chaotropic effect on water molecules altering its vibrational energy. Also, we outline that our data sets certainly underestimate the actual behavior due to our methodology. Along the thermal ramp, the water pressure increases, actively promoting connectivity, counteracting disorganization, and consequently attenuating the effects promoted by both $T$ and the interface.

**4.3. FTIR-Derived Thermodynamics of the Water−Solid Interface.** As mentioned in the previous section, the way the IR energy is absorbed by water offers many insights into its thermodynamic properties. Enthalpy ($H$) refers to the exchangeable thermal energy that can thermochemically accumulate in condensed matter through extension of the inner bonding network and the strength of this bonding. In that sense, the degree of molecular self-association is a measure of the enthalpy, meaning that undergoing a transition from a high to low degree of self-association (e.g., decreasing NW sub-band) requires that an enthalpic cost be paid. Entropy ($S$) measures the degree of order of matter and, therefore, relates to the degree of freedom of each molecule in an extended molecular network. An increasing degree of disorder means an increasing degree of freedom that has an IR expression in terms of enlarging the attainable level of energies, widening the corresponding band. Both properties, $H$ and $S$, are inter-related in terms of Gibbs free energy ($G$) by the relationship $G = H - TS$, so that variable $H$ and $S$ may compensate up to a nearly constant $G$, a well-studied effect for chemical reactions in biological systems.[80−82] According to the findings presented above, the bulk-to-interface water rearrangements qualitatively translate into an increased entropy and enthalpy, making it difficult to anticipate the change in Gibbs free energy.

We are hopeful that an independent path for calculating the Gibbs free energy is offered by the partition function developed recently.[16,57,70] It consists of summing the wavenumber of all of the inter- and intramolecular water modes to deduce the Gibbs free energy, assuming it depends on only the


https://doi.org/10.1021/acs.langmuir.4c00742
Langmuir XXXX, XXX, XXX−XXX

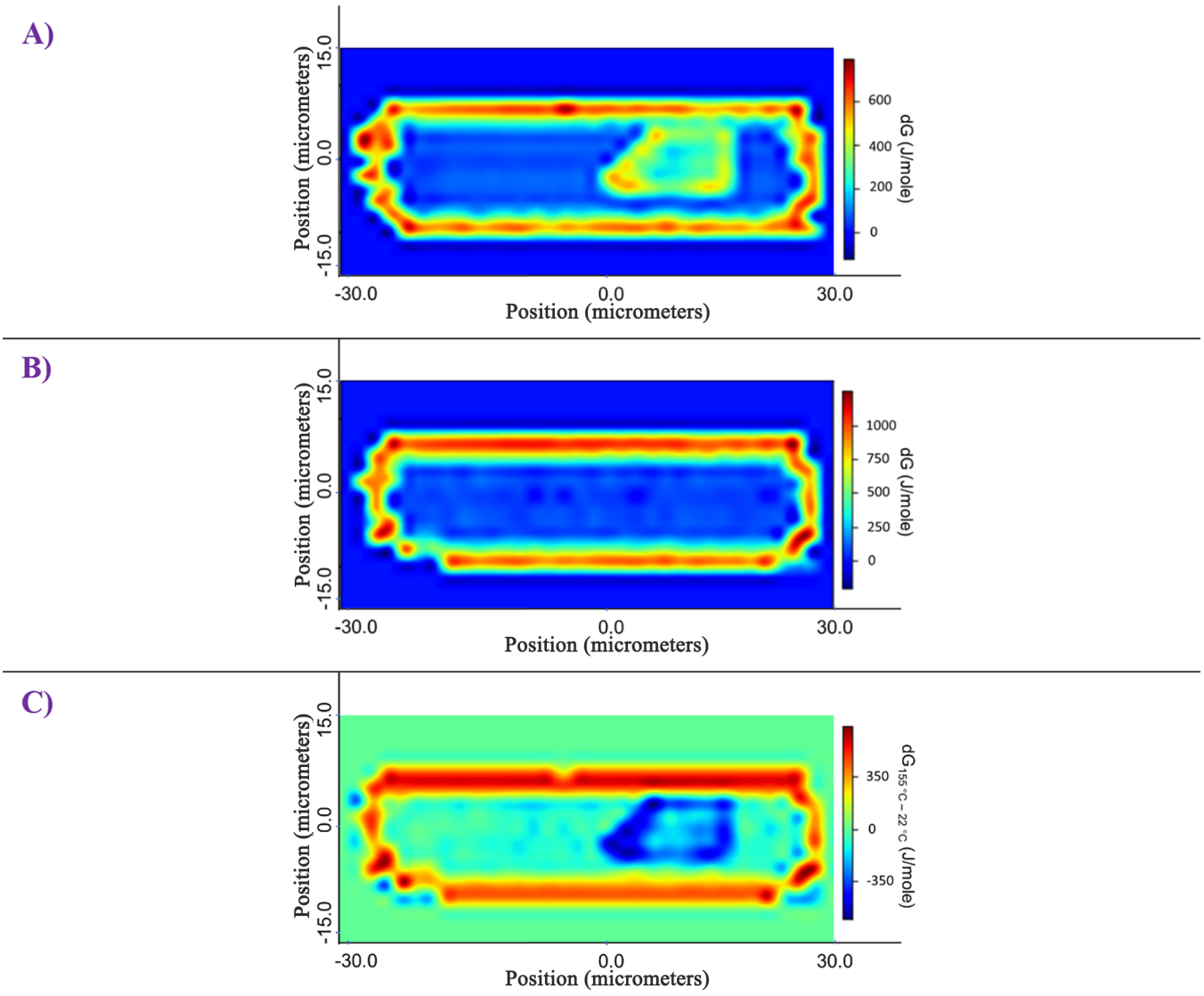


**Figure 12.** Maps of the variation of the Gibbs free energy all along SFI-1 at (A) RT and (B) $T_h$ (155 °C) and (C) differences between the Gibbs free energy at RT and $T_h$ (B minus A).

vibrational energy (see ref 57 for details and the Supporting Information for an overview of the equations).

As previously highlighted, our experimental setup allows us to exclusively record the intermolecular stretching band because of both the laser wavelength and the quartz cutoff wavenumber. As a result, the IR-to-thermodynamic conversion is performed assuming that all modes other than intramolecular stretching are not changing close to the walls and are taken to be equal to the values reported in the literature for liquid water as a function of temperature.[57,70,83] At 155 °C, for which no literature data are available, the values are extrapolated from what is known at lower temperatures (−10 to 90 °C) with $T$-dependent regressions.

The key characteristic of the conversion technique is calculating not an absolute value of the Gibbs free energy, but a variation relative to a reference situation (i.e., mean bulk water) to avoid the accumulation of uncertainties and imprecisions.[16,57] Consequently, the calculations showed the differences in the Gibbs free energy ($\Delta G$) from the center (i.e., bulk water) to the borders of SFI-1 (i.e., interfacial water). This relative approach affords a large value of $d\Delta G$ between the bulk and interface regions, which reaches 600 J/mol at RT (Figure 12A) and 1000 J/mol at $T_h$ (Figure 12B) over an almost similar thickness of 1 ± 0.5 $\mu$m. This method refines what can be deduced considering only the main peak change from one situation to another (see above).

Marechal[51,62] outlined the co-variation that is expected between the intramolecular stretching and the librations. The shift at markedly higher wavenumbers of the stretching band is associated with a decrease of its intensity point to weaker H-bonds. These weaker H-bonds persist with the appearance of the libration band at smaller wavenumbers (equivalent to librations of great amplitudes). Considering this proposition, we recalculated the Gibbs free energy of interfacial water with the same procedure described above but making the librations band diminish by 10% in wavenumber and 5% in absorbance at the bulk−interface transition. When this assumption is taken into account, the $d\Delta G$ between the bulk and interface regions shows a less pronounced variation by ∼30% (reaching 417 J/mol) at RT and by 34% (reaching 668 J/mol) at $T_h$.

For a clearer visualization of how $T$ enhances the interface effect, a point-by-point map of the difference in $d\Delta G$ between


https://doi.org/10.1021/acs.langmuir.4c00742
Langmuir XXXX, XXX, XXX−XXX

RT and $T_h$ was generated (Figure 12C), using only variation of the stretching band. In this representation, the bulk region is distinctly indicated by a uniform greenish color, underscoring that the bulk area remains unchanged between RT and $T_h$ and responds consistently to the temperature conditions. Undergoing a transition to the micrometer-thick interface region, the difference in $d\Delta G$ between RT and $T_h$ reaches 400 J/mol, indicating two significant findings. (i) Temperature enhances the interface effect but it does not spawn it, as the effect is discernible even at RT. (ii) The interface responds more dynamically to the temperature increment compared to bulk water. This observation, similar to a deduction drawn from the examination of sub-bands, but not evident from the NMF analysis, corresponds to a diminishing H-bond network in the interfacial region, with the predominance of the IW component. This shift is attributed to an enthalpic penalty incurred due to the hydrophobic effect. As a result, the shift from the bulk to interface is magnified with an increase in $T$, widening the gap between what is expected and what is experimentally measured.

Increasing the Gibbs free energy of a phase leads to modification of the solubility levels of any solid and gas reacting with water under such conditions. Additionally, this significant change in the chemical reactivity of liquid water takes place over a micrometer-thick domain, rather defining an interfacial domain than a sharp interface. In that respect, both the variation of the thermodynamic potential and the enormous amount of active water give us reasons to modify our view of a liquid−solid interaction on the multiphase boundary scale. Due to the thermal sensitivity of this interface-driven effect, the practical consequences of the water−rock interactions will be maximized for the high-$T$ diagenetic or hydrothermal processes.

## 5. CONCLUSION

In this investigation, we evaluated the effect of three physical and chemical parameters on the stability of the thick interface previously recorded[16,17] by micro-FTIR hyperspectral maps. The geometry of the cavity, the composition of the occluded solution, and the temperature were successively studied. This was achieved using a supercontinuum laser-based FTIR microspectroscopy technique applied to water occluded within SFIs in transmission mode. In a manner independent of cavity geometry, liquid composition, and temperature, the results show the presence of a ubiquitous micrometer-thick water layer with properties distinct from those of bulk water. The former layer is aligned all along the quartz−water edges, while the latter occupies the central volume of the cavity. This observation underscores the significance of the interfacial reaction zone, revealing a distinctive thermodynamic activity, contrary to conventional expectations. We have observed that interfacial water displays fewer hydrogen-bonded molecules than does bulk water (33% less well-connected water molecules at room temperature and 35% at 155 °C). We propose that this fact derives from interface-driven forces, specifically the hydrophobic force emanating from the solid boundary.

From a spectral point of view, the interfacial behavior of water was distinguished by an additional peak at ∼3700 $cm^{-1}$, which is attributed to the less connected water molecules in the water spectra. The molecular networking of interfacial water is dominated by IW (two- or three-connected molecules), a fact promoted by $T$, which is strikingly different from bulk water dominated by NW even at high $T$'s. Moreover, the peak at ∼3700 $cm^{-1}$ becomes more intense at high temperatures (≤155 °C), which means that temperature and wall proximity both have a chaotropic effect on the molecular networking of water by decreasing their coordination number.

Our findings suggest the existence of a surface force field associated with the presence of a solid boundary, capable of altering the energetic distribution within the molecular network of an interacting fluid. The statistical interpretation of the $T$-dependent experiment provides grounds for conceptualizing this spectrum-thick layer as the convolution of a true "physics-based" thinner layer with bulk water. In that sense, the recorded thickness would result from the relatively large size of the microbeam with respect to the underlying process(es). Only measurements at still better submicrometer resolution may clarify this hypothesis. Regardless of the correct interfacial sketch, water inside this region imparts less energy to the four-connected molecules compared to other H-bond configurations, thereby inducing a significant shift in the thermodynamic activity of liquid water. As already illustrated,[84] water at nonpolar surfaces is at a higher interfacial energy because the self-association of water is promoted while the surface water interactions are dominated by dispersive van der Waals forces. This yields an extended or open water structure at a density lower than that of bulk water, requiring that the H-bond network of interfacial water directly adjacent to a nonpolar surface be interrupted, giving rise to "dangling H-bonds" that are responsible for the large 3700 $cm^{-1}$ peak.

To quantify the reactivity of fluid−rock interactions along the multiphases, the thermodynamic properties were deduced from the FTIR spectral signature. The result reveals a micrometer-thick interphase region that may constitute a distinct domain with specific thermodynamic features. The Gibbs free energy of this domain is higher than that of the bulk, and this trend is enhanced by $T$. Water along hydrophobic interfaces is therefore more reactive (or less stable) than bulk water.

Overall, these findings lead us to conclude that the interphase domain should be involved in interpreting water−rock interactions in pores, channels, and cavities. The key aspect is that this interphase, in terms of both intensity and propagation scope scale, relates to the chemical nature of the pore walls, which is consistent with other recent findings.[15] Our data set points to paying attention to the hydrophilic−hydrophobic characteristics of the inner pore walls (i.e., solid surface chemistry), which cooperate in these synergistic in-pore processes as a prominent actor in the water−rock interactions and therefore of the mineral solubilities. Complementary studies based on hydrophilic and hydrophobic fluid inclusions are currently attempting to go beyond this inference to quantify the thermodynamic shift in terms of the hydrophobicity scale.

## ■ ASSOCIATED CONTENT

### Supporting Information

The Supporting Information is available free of charge at https://pubs.acs.org/doi/10.1021/acs.langmuir.4c00742.

Partition function for converting vibrational spectroscopy to thermodynamic properties and additional references (PDF)



https://doi.org/10.1021/acs.langmuir.4c00742
Langmuir XXXX, XXX, XXX−XXX

## AUTHOR INFORMATION


### Corresponding Author

**Armin Mozhdehei** − *Institut des Sciences de la Terre d'Orléans (ISTO) - UMR 7327 Université d'Orléans, CNRS, 45071 Orléans, France;* orcid.org/0000-0002-6389-8802; Email: arminm992@gmail.com

### Authors

**Lionel Mercury** − *Institut des Sciences de la Terre d'Orléans (ISTO) - UMR 7327 Université d'Orléans, CNRS, 45071 Orléans, France;* orcid.org/0000-0002-3825-663X

**Aneta Slodczyk** − *Institut des Sciences de la Terre d'Orléans (ISTO) - UMR 7327 Université d'Orléans, CNRS, 45071 Orléans, France; CEMHTI, UPR 3079 CNRS - Université d'Orléans, F-45071 Orléans, France*

Complete contact information is available at: https://pubs.acs.org/10.1021/acs.langmuir.4c00742


### Author Contributions

A.M.: conceptualization, investigation, validation, methodology, visualization, data curation, formal analysis, and writing of the original draft. L.M.: conceptualization, methodology, supervision, writing of the original draft, review and editing, project administration, funding acquisition, and resources. A.S.: supervision, investigation, methodology, data curation, and review and editing.

### Notes

The authors declare no competing financial interest.

## ACKNOWLEDGMENTS

This work has received financial support from the French Agency for Research (Agence Nationale de la Recherche), through Labex Voltaire ANR-10-LABX-100-01 and Equipex Planex ANR-11-EQPX-36. The authors are indebted to Arnault Lassin from BRGM (Orléans France) for his help with the quartz solubilities at high pH, performed with a BRGM-private version of the phreeSCALE database that includes Pitzer parameters for silica species absent from the open access version (DOI 10.18144/xy83-6848). The authors are also grateful to Raoul Missodey for developing the script of the NMF analysis.

## REFERENCES


(1) Azaroual, M.; Fouillac, C.; Matray, J. Solubility of silica polymorphs in electrolyte solutions, II. Activity of aqueous silica and solid silica polymorphs in deep solutions from the sedimentary Paris Basin. *Chem. Geol.* **1997**, *140* (3−4), 167−179.

(2) Kharaka, Y. K.; Mariner, R. H. Chemical geothermometers and their application to formation waters from sedimentary basins. In *Thermal history of sedimentary basins*; Springer, 1989; pp 99−117.

(3) Xiong, Q.; Baychev, T. G.; Jivkov, A. P. Review of pore network modelling of porous media: Experimental characterisations, network constructions and applications to reactive transport. *Journal of contaminant hydrology* **2016**, *192*, 101−117.

(4) Steefel, C. I.; MacQuarrie, K. T. Approaches to modeling of reactive transport in porous media. *Reactive transport in porous media* **1996**, 83−130.

(5) Abercrombie, H. J.; et al. Silica activity and the smectite-Illite reaction. *Geology* **1994**, *22* (6), 539−542.

(6) McBride, E. F. Quartz cement in sandstones: a review. *Earth-Science Reviews* **1989**, *26* (1−3), 69−112.

(7) Abd, A. S.; Abushaikha, A. S. Reactive transport in porous media: a review of recent mathematical efforts in modeling geochemical reactions in petroleum subsurface reservoirs. *SN Appl. Sci.* **2021**, *3* (4), 1−28.

(8) Putnis, A.; Mauthe, G. The effect of pore size on cementation in porous rocks. *Geofluids* **2001**, *1* (1), 37−41.

(9) Baermann, A.; et al. Anhydrite Cement in Rhaetian sandstone in Hamburg-Morphology and structures. *Z. Angew. Geol.* **2000**, *46* (3), 138−143.

(10) Gardeniers, H. J. Chemistry in nanochannel confinement. *Anal. Bioanal. Chem.* **2009**, *394* (2), 385−397.

(11) Le Caër, S.; et al. A trapped water network in nanoporous material: the role of interfaces. *Phys. Chem. Chem. Phys.* **2011**, *13* (39), 17658−17666.

(12) Tsukahara, T.; et al. NMR study of water molecules confined in extended nanospaces. *Angew. Chem.* **2007**, *119* (7), 1199−1202.

(13) Munoz-Santiburcio, D.; Marx, D. Confinement-controlled aqueous chemistry within nanometric slit pores: Focus review. *Chem. Rev.* **2021**, *121* (11), 6293−6320.

(14) Zheng, J.-m.; et al. Surfaces and interfacial water: evidence that hydrophilic surfaces have long-range impact. *Advances in colloid and interface science* **2006**, *127* (1), 19−27.

(15) Stack, A. G.; et al. Pore-size-dependent calcium carbonate precipitation controlled by surface chemistry. *Environ. Sci. Technol.* **2014**, *48* (11), 6177−6183.

(16) Bergonzi, I.; et al. Oversolubility in the microvicinity of solid−solution interfaces. *Phys. Chem. Chem. Phys.* **2016**, *18* (22), 14874−14885.

(17) Mozhdehei, A.; et al. Diffraction-limited mid-infrared microspectroscopy to reveal a micron-thick interfacial water layer signature. *Analyst* **2023**, *148*, 2941.

(18) Roedder, E. Studies of fluid inclusions;[Part] 2, Freezing data and their interpretation. *Economic geology* **1963**, *58* (2), 167−211.

(19) Roedder, E. Metastable superheated ice in liquid-water inclusions under high negative pressure. *Science* **1967**, *155* (3768), 1413−1417.

(20) Roedder, E. *Fluid Inclusions* **1984**, *12*, n/a.

(21) Shmulovich, K. I.; Graham, C. M. An experimental study of phase equilibria in the systems H 2 O−CO 2−CaCl 2 and H 2 O−CO 2−NaCl at high pressures and temperatures (500−800° C, 0.5−0.9 GPa): geological and geophysical applications. *Contributions to Mineralogy and Petrology* **2004**, *146* (4), 450−462.

(22) Shmulovich, K. I.; et al. Experimental superheating of water and aqueous solutions. *Geochim. Cosmochim. Acta* **2009**, *73* (9), 2457−2470.

(23) Shmulovich, K.; Yardley, B.; Graham, C. Solubility of quartz in crustal fluids: experiments and general equations for salt solutions and H2O−CO2 mixtures at 400−800 C and 0.1−0.9 GPa. *Geofluids* **2006**, *6* (2), 154−167.

(24) Jamme, F.; et al. Synchrotron infrared confocal microscope: Application to infrared 3D spectral imaging. *Journal of Physics: Conference Series* **2013**, *425* (14), No. 142002.

(25) Lavoute, L.; et al. Mid-Infrared Spectromicroscopy with a Supercontinuum Laser Source. In *Specialty Optical Fibers*; Optical Society of America, 2016.

(26) Dudley, J. M.; Genty, G.; Coen, S. Supercontinuum generation in photonic crystal fiber. *Reviews of modern physics* **2006**, *78* (4), 1135.

(27) Hurai, V.; et al. *Geofluids: developments in microthermometry, spectroscopy, thermodynamics, and stable isotopes*; Elsevier, 2015.

(28) Mercury, L.; et al. Growing Negative Pressure in Dissolved Solutes: Raman Monitoring of Solvent-Pulling Effect. *J. Phys. Chem. C* **2016**, *120* (14), 7697−7704.

(29) Fall, A.s.; Rimstidt, J. D.; Bodnar, R. J. The effect of fluid inclusion size on determination of homogenization temperature and density of liquid-rich aqueous inclusions. *Am. Mineral.* **2009**, *94* (11−12), 1569−1579.

(30) Wagner, W.; Pruß, A. The IAPWS formulation 1995 for the thermodynamic properties of ordinary water substance for general and scientific use. *Journal of physical and chemical reference data* **2002**, *31* (2), 387−535.

(31) Mürmann, M.; et al. Numerical simulation of pore size dependent anhydrite precipitation in geothermal reservoirs. *Energy Procedia* **2013**, *40*, 107−116.
(32) Wu, J. Understanding the electric double-layer structure, capacitance, and charging dynamics. *Chem. Rev.* **2022**, *122* (12), 10821−10859.
(33) Wang, G.; Brown, W.; Kvetny, M. Structure and dynamics of nanoscale electrical double layer. *Current Opinion in Electrochemistry* **2019**, *13*, 112−118.
(34) Felmy, A. R.; et al. An aqueous thermodynamic model for polymerized silica species to high ionic strength. *J. Solution Chem.* **2001**, *30*, 509−525.
(35) Lach, A.; et al. A new Pitzer parameterization for the binary NaOH−H 2 O and ternary NaOH−NaCl−H 2 O and NaOH−LiOH−H 2 O systems up to NaOH solid salt saturation, from 273.15 to 523.15 K and at saturated vapor pressure. *J. Solution Chem.* **2015**, *44*, 1424−1451.
(36) André, L.; Lassin, A.; Lach, A. *PHREESCALE. DAT: A thermodynamic database for the PhreeSCALE software*, ver. 1.0; 2020.
(37) Du, Q.; Freysz, E.; Shen, Y. R. Vibrational spectra of water molecules at quartz/water interfaces. *Phys. Rev. Lett.* **1994**, *72* (2), 238.
(38) Dewan, S.; Yeganeh, M. S.; Borguet, E. Experimental correlation between interfacial water structure and mineral reactivity. *J. Phys. Chem. Lett.* **2013**, *4* (11), 1977−1982.
(39) Doshi, D. A.; et al. Reduced water density at hydrophobic surfaces: Effect of dissolved gases. *Proc. Natl. Acad. Sci. U. S. A.* **2005**, *102* (27), 9458−9462.
(40) Zhang, L.; et al. The morphology and stability of nanoscopic gas states at water/solid interfaces. *ChemPhysChem* **2012**, *13* (8), 2188−2195.
(41) Fang, C.-K.; et al. Nucleation processes of nanobubbles at a solid/water interface. *Sci. Rep.* **2016**, *6* (1), 24651.
(42) Vogel, P.; et al. Charging of Dielectric Surfaces in Contact with Aqueous Electrolytes—the Influence of $CO_2$. *J. Am. Chem. Soc.* **2022**, *144* (46), 21080−21087.
(43) Vogel, P.; Palberg, T. Electrokinetic effects of ambient and excess carbonization of dielectric surfaces in aqueous environments. *J. Colloid Interface Sci.* **2024**, *656*, 280−288.
(44) Brenner, M. P.; Lohse, D. Dynamic equilibrium mechanism for surface nanobubble stabilization. *Physical review letters* **2008**, *101* (21), No. 214505.
(45) Willard, A. P.; Chandler, D. The molecular structure of the interface between water and a hydrophobic substrate is liquid-vapor like. *J. Chem. Phys.* **2014**, *141* (18), 18C519.
(46) Mørch, K. A.; et al. Cavitation nuclei and surface nanobubbles: The model of non-adsorbed interfacial liquid zones. *Phys. Fluids* **2022**, *34* (12), 121707.
(47) Brubach, J.-B.; et al. Signatures of the hydrogen bonding in the infrared bands of water. *J. Chem. Phys.* **2005**, *122* (18), No. 184509.
(48) Freda, M.; et al. Transmittance Fourier transform infrared spectra of liquid water in the whole mid-infrared region: temperature dependence and structural analysis. *Applied spectroscopy* **2005**, *59* (9), 1155−1159.
(49) Larouche, P.; Max, J.-J.; Chapados, C. Isotope effects in liquid water by infrared spectroscopy. II. Factor analysis of the temperature effect on H 2 O and D 2 O. *J. Chem. Phys.* **2008**, *129* (6), No. 064503.
(50) Libnau, F. O.; et al. Spectra of water in the near-and mid-infrared region. *Vib. Spectrosc.* **1994**, *7* (3), 243−254.
(51) Maréchal, Y. Infrared spectra of water. I. Effect of temperature and of H/D isotopic dilution. *J. Chem. Phys.* **1991**, *95* (8), 5565−5573.
(52) Gaweł, B. A.; et al. Structural evolution of water and hydroxyl groups during thermal, mechanical and chemical treatment of high purity natural quartz. *RSC Adv.* **2020**, *10* (48), 29018−29030.
(53) Gaweł, B. A.; et al. In situ high temperature spectroscopic study of liquid inclusions and hydroxyl groups in high purity natural quartz. *Minerals Engineering* **2021**, *174*, No. 107238.
(54) Zhou, L.; Mernagh, T. P.; Le Losq, C. Observation of the Chemical Structure of Water up to the Critical Point by Raman Spectroscopic Analysis of Fluid Inclusions. *J. Phys. Chem. B* **2019**, *123* (27), 5841−5847.
(55) Yasaka, Y.; et al. High-sensitivity Raman spectroscopy of supercritical water and methanol over a wide range of density. *Bull. Chem. Soc. Jpn.* **2007**, *80* (9), 1764−1769.
(56) Frantz, J. D.; Dubessy, J.; Mysen, B. An optical cell for Raman spectroscopic studies of supercritical fluids and its application to the study of water to 500 C and 2000 bar. *Chem. Geol.* **1993**, *106* (1−2), 9−26.
(57) Bergonzi, I.; et al. Gibbs free energy of liquid water derived from infrared measurements. *Phys. Chem. Chem. Phys.* **2014**, *16* (45), 24830−24840.
(58) Nieuwoudt, M. K.; et al. Synchrotron FTIR microscopy of synthetic and natural $CO_2$−$H_2O$ fluid inclusions. *Vib. Spectrosc.* **2014**, *75*, 136−148.
(59) Walrafen, G.; Hokmabadi, M.; Yang, W. H. Raman isosbestic points from liquid water. *J. Chem. Phys.* **1986**, *85* (12), 6964−6969.
(60) Walrafen, G.; et al. Temperature dependence of the low-and high-frequency Raman scattering from liquid water. *J. Chem. Phys.* **1986**, *85* (12), 6970−6982.
(61) Geissler, P. L. Temperature dependence of inhomogeneous broadening: On the meaning of isosbestic points. *J. Am. Chem. Soc.* **2005**, *127* (42), 14930−14935.
(62) Maréchal, Y. The molecular structure of liquid water delivered by absorption spectroscopy in the whole IR region completed with thermodynamics data. *J. Mol. Struct.* **2011**, *1004* (1−3), 146−155.
(63) Esposito, F. A review on initialization methods for nonnegative matrix factorization: towards omics data experiments. *Mathematics* **2021**, *9* (9), 1006.
(64) Feng, X.-R.; et al. Hyperspectral unmixing based on nonnegative matrix factorization: A comprehensive review. *IEEE Journal of Selected Topics in Applied Earth Observations and Remote Sensing* **2022**, *15*, 4414.
(65) Muto, S.; Shiga, M. Application of machine learning techniques to electron microscopic/spectroscopic image data analysis. *Microscopy* **2020**, *69* (2), 110−122.
(66) Shiga, M.; Muto, S. Non-negative matrix factorization and its extensions for spectral image data analysis. *E-Journal of Surface Science and Nanotechnology* **2019**, *17*, 148−154.
(67) Pauca, V. P.; Piper, J.; Plemmons, R. J. Nonnegative matrix factorization for spectral data analysis. *Linear algebra and its applications* **2006**, *416* (1), 29−47.
(68) Boissiere, C.; et al. Water confined in lamellar structures of AOT surfactants: an infrared investigation. *J. Phys. Chem. B* **2002**, *106* (5), 1032−1035.
(69) Onori, G.; Santucci, A. IR investigations of water structure in aerosol OT reverse micellar aggregates. *J. Phys. Chem.* **1993**, *97* (20), 5430−5434.
(70) Bergonzi, I.; Mercury, L. Infrared-Thermodynamics conversion as a function of temperature: towards confined water. In *Transport and Reactivity of Solutions in Confined Hydrosystems*; Springer, 2014; pp 43−53.
(71) Knight, A. W.; et al. Water properties under nano-scale confinement. *Sci. Rep.* **2019**, *9* (1), 8246.
(72) Hester, R. E. *Advances in infrared and Raman spectroscopy*; Heyden, 1977.
(73) Du, Q.; et al. Vibrational spectroscopy of water at the vapor/water interface. *Phys. Rev. Lett.* **1993**, *70* (15), 2313.
(74) Kretzschmar, K.; et al. An IR study of the adsorption of water on Ru (001). *Surf. Sci.* **1982**, *115* (1), 183−194.
(75) Wernet, P.; et al. The structure of the first coordination shell in liquid water. *Science* **2004**, *304* (5673), 995−999.
(76) Auer, B.; et al. Hydrogen bonding and Raman, IR, and 2D-IR spectroscopy of dilute HOD in liquid D2O. *Proc. Natl. Acad. Sci. U. S. A.* **2007**, *104* (36), 14215−14220.
(77) Chandler, D. Interfaces and the driving force of hydrophobic assembly. *Nature* **2005**, *437* (7059), 640−647.


https://doi.org/10.1021/acs.langmuir.4c00742
*Langmuir* XXXX, XXX, XXX−XXX

(78) Takei, T.; et al. Changes in density and surface tension of water in silica pores. *Colloid Polym. Sci.* **2000**, *278* (5), 475−480.
(79) Etzler, F. M. Enhancement of hydrogen bonding in vicinal water; heat capacity of water and deuterium oxide in silica pores. *Langmuir* **1988**, *4* (4), 878−883.
(80) Dunitz, J. D. Win some, lose some: enthalpy-entropy compensation in weak intermolecular interactions. *Chemistry & biology* **1995**, *2* (11), 709−712.
(81) Starikov, E. B.; Nordén, B. Enthalpy− entropy compensation: a phantom or something useful? *J. Phys. Chem. B* **2007**, *111* (51), 14431−14435.
(82) Dragan, A. I.; Read, C. M.; Crane-Robinson, C. Enthalpy−entropy compensation: the role of solvation. *Eur. Biophys. J.* **2017**, *46* (4), 301−308.
(83) Adam, N. K. Properties of ordinary water-substance in all its phases. *Nature* **1940**, *146*, 145−146.
(84) Vogler, E. A. Structure and reactivity of water at biomaterial surfaces. *Advances in colloid and interface science* **1998**, *74* (1−3), 69−117.


https://doi.org/10.1021/acs.langmuir.4c00742
*Langmuir* XXXX, XXX, XXX−XXX